

See discussions, stats, and author profiles for this publication at: <https://www.researchgate.net/publication/7954983>

“Zn-Link”: A Metal-Sharing Interface that Organizes the Quaternary Structure and Catalytic Site of the Endoribonuclease, RNase E †

ARTICLE *in* BIOCHEMISTRY · APRIL 2005

Impact Factor: 3.02 · DOI: 10.1021/bi0478244 · Source: PubMed

CITATIONS

35

READS

32

11 AUTHORS, INCLUDING:



Jörg Günter Grossmann

University of Liverpool

145 PUBLICATIONS 4,198 CITATIONS

[SEE PROFILE](#)



Elspeth F Garman

University of Oxford

175 PUBLICATIONS 6,567 CITATIONS

[SEE PROFILE](#)



Leopold L Ilag

Stockholm University

61 PUBLICATIONS 1,536 CITATIONS

[SEE PROFILE](#)



Kenneth J Mcdowall

University of Leeds

29 PUBLICATIONS 1,137 CITATIONS

[SEE PROFILE](#)

“Zn-Link”: A Metal-Sharing Interface that Organizes the Quaternary Structure and Catalytic Site of the Endoribonuclease, RNase E[†]

Anastasia J. Callaghan,[‡] Yulia Redko,[§] Loretta M. Murphy,^{||} J. Günter Grossmann,[⊥] David Yates,[#] Elspeth Garman,[#] Leopold L. Ilag,^{||} Carol V. Robinson,^{||} Martyn. F. Symmons,[‡] Kenneth J. McDowall,[§] and Ben F. Luisi^{*‡}

Department of Biochemistry, University of Cambridge, Cambridge CB2 1GA, United Kingdom, Astbury Centre for Structural Molecular Biology, University of Leeds, Leeds LS2 9JT, United Kingdom, Department of Chemistry, University of Wales Bangor, Bangor, LL57 2UW, United Kingdom, CCLRC Daresbury Laboratory, Daresbury, Warrington WA4 1AD, United Kingdom, Department of Biochemistry, University of Oxford, Oxford OX1 3QU, United Kingdom, and Department of Chemistry, University of Cambridge, Cambridge CB2 1EW, United Kingdom

Received October 8, 2004; Revised Manuscript Received November 28, 2004

ABSTRACT: Ribonuclease E is an essential hydrolytic endonuclease in *Escherichia coli*, and it plays a central role in maintaining the balance and composition of the messenger RNA population. The enzyme is also required for rRNA and tRNA processing. We have shown earlier that the highly conserved catalytic domain of *E. coli* RNase E is a homotetramer [Callaghan, A. J. et al. (2003) *Biochemistry* 42, 13848–13855]. Here, we report that this quaternary organization requires zinc. Two protomers share a single zinc ion, and quantitative analysis indicates that each protein contributes two cysteine thiols toward the coordination of the metal. The candidate cysteines are part of a motif that is conserved in the RNase E protein family, and mutation of these residues causes the partial loss of zinc, the complete disruption of the tetramer into dimers, and effective catalytic inactivation. However, these mutations do not affect RNA binding. The tetramer can be artificially maintained by disulfide bond formation, which fully displaces the zinc but largely preserves the catalytic activity. Thus, catalytic activity does not require zinc directly but does require the quaternary structure, for which the metal is essential. We propose that the RNase E tetramer has two nonequivalent subunit interfaces, one of which is mediated by a single, tetrathiol–zinc complex, which we refer to as a “Zn-link” motif. One or both interfaces organize the active site, which is distinct from the primary site of RNA binding.

Under steady-state growth conditions, transcript levels remain relatively constant through the balance of synthesis and decay, and these levels are regulated by diverse mechanisms. At the post-transcriptional stage, the turnover of messenger RNA and other RNA species affects the duration of gene expression. Among all domains of life, this turnover is mediated by endo- and exoribonucleases. In *Escherichia coli*, the endonucleolytic ribonuclease RNase E plays an essential role in regulating the balance and composition of the transcripts (1, 2). Indeed, temperature-sensitive mutants of RNase E have been shown to affect the decay of bulk mRNA and rRNA (3), causing an increase in their half-lives under nonpermissive conditions (4). RNase E has also been shown to be responsible for initiating the decay of most transcripts in *E. coli* (5–8). Additionally, RNase E has a number of other important roles including

the generation of transfer and ribosomal RNAs from larger precursors, the catalytic RNA of RNase P, and the transfer/messenger RNA (tmRNA) that rescues stalled ribosomes (9–11).

RNase E is one of the largest proteins encoded in *E. coli*, and its 1061 residues can be divided into domains of defined function and structure (Figure 1). The highly conserved ribonuclease E N-terminal catalytic domain (NTD)¹ corresponds to roughly the first half of the protein (12). This domain appears to be sufficient for cell viability (13), and homologues have been found in bacteria, archaea, plastids, and some higher plant species (14–17). *E. coli* RNase G is a paralogue of the RNase E NTD that has been found to also have endoribonuclease activity but is nonessential and appears to have a role in the decay of a relatively limited number of transcripts and in the generation of 16S rRNA (18–23).

The carboxy-terminal half of RNase E (CTD) is highly divergent among RNase E homologues and, in some cases, is completely lacking, so that the enzymes more closely

[†] This study was supported by the Wellcome Trust and a grant from the BBSRC.

* To whom correspondence should be addressed. E-mail: ben@cryst.bioc.cam.ac.uk. Fax: 44-1223-766002. Telephone: 44-1223-766019.

[‡] Department of Biochemistry, University of Cambridge.

[§] University of Leeds.

^{||} University of Wales.

[⊥] CCLRC Daresbury Laboratory.

[#] University of Oxford.

[†] Department of Chemistry, University of Cambridge.

¹ Abbreviations: microPIXE, microbeam particle-induced X-ray emission; EXAFS, extended X-ray absorption fine structure; AUC, analytical ultracentrifugation; ESI, electrospray ionization; NTD, ribonuclease E N-terminal catalytic domain; PNPase, polynucleotide phosphorylase; BVS, bond valence sum analysis.

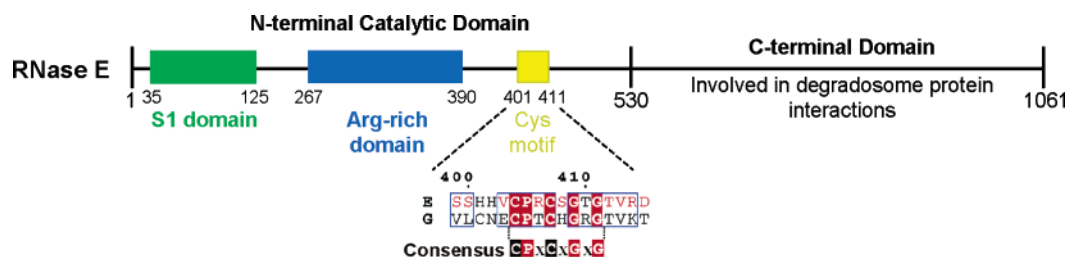


FIGURE 1: *E. coli* RNase E can be divided into domains of defined function and structure. The colored boxes illustrate the conserved regions with the residue numbers indicated. The C-terminal domain is involved in component interactions with the degradosome proteins (27–29, 56, 57). In the N-terminal domain, the S1 RNA-binding domain is shown in green; the Arg-rich domain, in blue; and the Cys motif, in yellow. For the Cys motif, bacterial RNase E sequences were aligned with those of *E. coli* RNase E and RNase G using ClustalW (58). For clarity, only the later two are shown, upper and lower sequences labeled E and G, respectively, and numbered with respect to *E. coli* RNase E. The sequences are grouped into RNases E and G separately and formatted with ESPript (59). Regions of global similarity between the E and G sequences are represented by the blue boxes [Riesler substitution matrix (59) with a similarity score of better than 60%], and residues that are identical are highlighted in red. Residues considered similar throughout the RNase E examples alone are shown in red (Riesler matrix but with a 70% threshold). Conserved Cys positions are highlighted in black within the consensus sequence of the Cys motif. Sequences used in the alignment and color scheme but not shown here were from *Salmonella typhi*, *Haemophilus influenzae*, *Neisseria meningitidis*, *Pseudomonas aeruginosa*, *Xylella fastidiosa*, *Xanthomonas axonopodis*, *Yersinia pestis*, *Pasteurella multocida*, *Vibrio cholerae*, and *Buchinera aphidicola*.

resemble RNase G (24, 25). The CTD serves as the scaffold for a multicomponent assembly, known as the RNA degradosome (14, 26). The principal proteins of the degradosome are the phosphorolytic exoribonuclease, polynucleotide phosphorylase (PNPase), the ATP-dependent RNA helicase RhlB, and the glycolytic enzyme enolase (27–29). The association of these enzymes into one complex provides cooperation of their activities, and it has been inferred that this cooperativity gives rise to targeted activity toward specific transcript classes (30). Although the domain is highly divergent among RNase E homologues, there is evidence that in other species the domain still serves as a platform for the assembly of multi-enzyme complexes. In *Streptomyces coelicolor*, the domain arrangement is shuffled such that the PNPase-binding scaffold regions are present at both ends of the protein and the domain homologous to the *E. coli* RNase E NTD is in the center of the protein (25).

We have previously shown that the RNase E NTD, which encompasses the site of catalytic activity, is globular and forms a homotetramer (31). Among the known domains in this region are the S1 RNA-binding motif and another highly conserved region that is rich in arginine. Recently, the structure of the RNase E S1 domain (residues 35–125) has been determined (32), and in general agreement with predictions made Diwa et al. (33), the domain has been shown to associate with single-stranded oligonucleotide. Likewise, photo-cross-linking experiments (Callaghan et al., manuscript in preparation) using the NTD identified the S1 domain as the site of contact with a 10-mer 2'-O-methyl RNA derived from the cleavage site of the anti-sense RNAI molecule of *E. coli* (34, 35). The 5' end of the RNA substrate has an important effect on catalysis (36), but it does not appear to be due to direct binding. Jiang and Belasco (37) have shown that the RNase E catalytic activity is greater for substrates with a free 5' monophosphate compared with those having a 5'-OH group, although both are bound with similar affinities. This suggests that the 5' end might affect the organization of the catalytic site.

In comparing the sequence of RNase E and its homologues, we noted the conservation of a pattern at residues 404–410. This pattern, CPXCXGXG, is also found in the metal-coordinating sites of the chaperone DnaJ and MutM (PDB entry 1EXK and 1EE8), where two intramolecular

copies of the pattern are used to coordinate a single zinc ion in a tetrathiol arrangement. These observations led us to investigate whether the motif might play a similar role in metal binding in RNase E. Because RNase E contains only a single copy of the pattern, we reasoned that two protomers could generate a binding site by sharing a metal between them. The metal would thus link two protomers, and we refer to this shared-metal interface as a “Zn-link”.

Here, we use a number of techniques to analyze the role of metal in the structure and function of *E. coli* RNase E. Using synchrotron X-ray fluorescence, we show that the protein does indeed contain zinc; no other candidate metals were found. The zinc stoichiometry is established using a technique of spectroscopic emission induced by a proton microbeam: particle-induced X-ray emission (microPIXE). We also use extended X-ray absorption fine structure spectroscopy (EXAFS) to identify the ligating atoms, and these data are consistent with a tetrathiol coordination scheme expected for metal coordination by four cysteine side chains. While the wild-type protein forms a stable homotetramer, the substitution of the conserved cysteines of the putative zinc coordination site with alanine result in disruption of the tetramer into stable dimers. Interestingly, these mutants have little catalytic activity toward the defined substrate, but they still retain the capacity to bind RNA, as shown by nondissociating nanoflow-electrospray ionization (ESI) mass spectrometry. This is consistent with the proposal that the S1 motif is the RNA-binding surface (32) and that it lies on the periphery of the RNase E tetramer, where it functions independently of the subunit interfaces (31). When these data are taken together, they are consistent with a model in which the RNase E tetramer is arranged around two nonequivalent interfaces. RNA binding does not require the zinc-mediated interface, but the organization of the catalytic site does.

MATERIALS AND METHODS

Purification of Wild-Type and Mutant RNase E NTD. The wild-type and mutant recombinant proteins were expressed and purified as described previously (31).

Site-Directed Mutagenesis. The cysteine residues at positions 404 and 407 in recombinant NTD were changed individually to alanine using the QuikChange Site-Directed

Mutagenesis kit (Stratagene). The oligonucleotides used were 5'-CAG TCA TCA CGT TGC TCC GCG TTG TTC TG, with its reverse complement 5'-CA GAA CAA CGC GGA GCA ACG TGA TGA CTG, and 5'-CGT TTG TCC GCG TGC TTC TGG TAC TGG C, with its reverse complement 5'-G CCA GTA CCA GAA GCA CGC GGA CAA ACG. Changes introduced into the cysteines codons are underlined. The presence of these mutations in the corresponding expression construct pRne529-N (31) was confirmed by sequencing (DBS Genomics, University of Durham, U.K.).

Diamide Treatment of RNase E NTD. To assay the effect of diamide on the activity of NTD, samples of the enzyme (40–400 nM) in reaction buffer (25 mM Bis-Tris-propane-HCl at pH 8.3, 100 mM NaCl, 15 mM MgCl₂, and 0.1% (v/v) Triton X-100) containing 2 mM diamide were incubated at 37 °C for 1 h. Aliquots of appropriate amounts were then mixed with the substrate in reaction buffer also containing 2 mM diamide. The reaction conditions and assay procedure were as described previously (38).

To determine the effects on zinc binding, diamide was added to a 500 μ L aliquot of the NTD (50 μ M) to a final concentration of 2 mM and the sample incubated at 37 °C for 1 h and then dialyzed overnight against 50 mM Tris-HCl (pH 8.0) and 500 mM NaCl using a Spectra/Por Dialyzer with a MWCO of 1000 (Spectrum Labs). The sample was then frozen at –80 °C until analyzed by microPIXE.

Analytical Size-Exclusion Chromatography. Samples of NTD (typically 100 μ L of 10–20 μ M) were run on a Sephacryl S-200 HR column (1.6 \times 60 cm, Amersham Biosciences) using a Bio-CAD SPRINT system (Perceptive Biosystems). The column was equilibrated with running buffer (50 mM Tris-HCl at pH 8.0 and 400 mM NaCl) and calibrated with a molecular weight marker kit for gel-filtration chromatography (Sigma).

Analytical Ultracentrifugation. Samples of NTD wild type or mutants were dialyzed overnight at 4 °C against 50 mM Tris (pH 8.0), 400 mM NaCl, 15 mM MgCl₂, and 10 mM dithiothreitol (DTT). Diamide-treated samples were dialyzed against 50 mM Tris-HCl (pH 8.0) and 400 mM NaCl. A Beckman Optima XL-I analytical ultracentrifuge (Beckman Coulter) with an interference optical system was used. Sedimentation velocity data were collected and analyzed as described previously (31). The concentration of the samples was typically 50 μ M. Samples of bovine serum albumin (BSA) and α amylase were also analyzed for comparative purposes.

Oligonucleotide Synthesis. The RNA substrates used were as detailed previously (31, 38). For enzymatic assays, the RNA decamer ACAGUAUUUG with a 5' monophosphate and 3' fluorescein was used. Similarly, for RNA-binding experiments, the same RNA was used but was synthesized with protective 2'-O-methyl groups at all positions.

Enzymatic Activity and Electrophoretic Mobility Assays. Enzyme activity assays were carried out as detailed previously (38). For the electrophoretic mobility assays, the RNA tridecamer GGGACAGUAUUUG with a 5'-monophosphate and protective 2'-O-methyl groups at all positions was used.

Nanoflow-ESI Mass Spectrometry. Samples of wild-type, C404A, C407A, and diamide-treated NTD were buffer-exchanged into 1 M ammonium acetate (Micro Bio-Spin chromatography columns, Bio-Rad). Mass spectra for the proteins (~3 mg/mL) and the protein–RNA complex (3 mg/

mL protein with 2-fold stoichiometric excess of RNA) were collected on a modified Q-ToF2 mass spectrometer (39) equipped with a nanoflow Z-spray source (Micromass). Data were collected and processed as detailed previously (31, 40).

Proton-Induced X-ray Emission. The microPIXE measurements were carried out at the National Ion Beam Centre, University of Surrey, U.K., on a beamline arranged as described previously (41). The protein was buffer-exchanged into 0.5 M ammonium acetate, and approximately 0.2 μ L of protein or buffer control were each pipetted onto two separate 2 μ m thick Mylar films in aluminum target holders and dried, as described previously (42). A 2–3 MeV proton beam of 1 μ m in diameter was used to induce characteristic X-ray emission from the dried liquid droplet under vacuum. The X-rays were detected in a solid-state lithium-drifted silicon detector with high energy resolution. The proton beam was then scanned spatially in the *x* and *y* dimensions of the target. Using the data collection software, spatial maps were obtained of all elements heavier than neon that were present in the sample. Quantitative information was obtained by collecting spectra at selected points on the drop and also at a point on the backing foil. These spectra were analyzed using GUPIX (43) to extract the areal density of each element of interest in the sample.

X-ray Fluorescence Spectroscopy and X-ray Absorption Spectroscopy (XAS). The Zn K-edge X-ray absorption data and X-ray fluorescence spectra were recorded on Station 16.5 at the Synchrotron Radiation Source, Daresbury Laboratory, U.K. Monochromatic light was provided by a Si (220) double-crystal sagittal monochromator, which was adjusted throughout the energy scan to maintain a constant spot size. The energy was calibrated using a 5 μ m zinc foil, taking the point of inflection to be 9659 eV. The X-ray beam dimensions on the sample were 4 mm (width) \times 2.5 mm (height). Data were recorded in fluorescence mode on a 30 element Ge Solid State Detector (44).

X-ray fluorescence spectra were obtained for NTD (for a ~5 mg/mL sample) and a buffer-matched sample. The solid-state fluorescence detector output channel positions were calibrated in energy against zinc and vanadium foils. The monochromator was moved to 10.3 keV (above the zinc edge) and the X-ray fluorescence profile for protein and buffer blank were recorded for 120 s each.

For EXAFS measurements, approximately 100 μ L of NTD at 33 mg/mL in 50 mM Tris at pH 7.9, 300 mM NaCl, 10 mM MgCl₂, 5 mM DTT, and 5% glycerol was loaded into a Perspex sample cell (central aperture of 20 \times 4 \times 1.5 mm³, covered with 25 μ m Mylar). The sample was frozen in liquid nitrogen and transferred to a coldfinger “bucket” cryostat to keep the sample at roughly 80 K throughout data collection. Four scans were recorded and then summed, reweighted, and calibrated using EXCALIB (45). Background subtraction and normalization were performed using EXBACK (45). The EXAFS data analysis was performed using EXCURVE (46) with fast curved wave (or Rehr–Albers) theory, including up to a third-order multiple scattering contributions. The data were fitted over the *k* range of 2.65–11.9 Å^{–1}. Phase shifts were calculated in EXCURVE using von Barth for the ground-state exchange term and Hedin–Lundqvist for the excited-state exchange term.

Initial models used single-scattering theory to fit the inner shell(s). Subsequent fits, which extended the models to

include the outer shells of atoms, included multiple scattering contributions and used constrained refinement methods (47, 48). Bond valence sum analysis (BVS) was performed using VALENCE (49).

The quality of the fit of theoretical EXAFS of a model to the experimental data can be assessed quantitatively using the Fit index (ϕ_{EXAFS}), R factor (R_{EXAFS}) and reduced χ^2 function (ϵ_v^2). The Fit index (the parameter that is minimized during the least-squares refinement) is of the sum of the square of residuals

$$\phi_{\text{EXAFS}} = \sum_i^N w_i^2 (\chi_i^{\text{exp}}(k) - \chi_i^{\text{th}}(k))^2 \quad (1)$$

where $\chi^{\text{exp}}(k)$ and $\chi^{\text{th}}(k)$ are the experimental and theoretical EXAFS respectively, and

$$w_i = \frac{k_i^n}{\sum_j^N k_j^n |\chi_j^{\text{exp}}(k_j)|} \quad (2)$$

for which $n = 3$ in the data analysis presented here.

R_{EXAFS} gives an indication of the quality of fit in k space

$$R_{\text{EXAFS}} = \sum_i^N w_i (|\chi_i^{\text{exp}}(k) - \chi_i^{\text{th}}(k)|) \times 100\% \quad (3)$$

ϕ_{EXAFS} and R_{EXAFS} do not take into account either the number of parameters that have been refined (N_{pars}) or the number of independent data points (N_{ind}). However, ϵ_v^2 gives an indication of the overall goodness of fit, which takes into account the degree of over-determination of the system. Reduced χ^2 is not an absolute value but relative and thus can be used to decide which is the best statistical fit

$$\epsilon_v^2 = \left[\frac{1}{(N_{\text{ind}} - N_{\text{pars}})} \right] \left(\frac{N_{\text{ind}}}{N} \right) \sum_i^N w_i (\chi_i^{\text{exp}}(k) - \chi_i^{\text{th}}(k))^2$$

where

$$N_{\text{ind}} = \frac{2\Delta k \Delta R}{\pi} + 1 \quad (4)$$

Δk is the data range being fitted in k space (between k_{min} and k_{max}), and ΔR is the range of data being fitted in R space (between R_{min} and R_{max}) by the model where the data are substantial.

For each model the interatomic distance, Debye–Waller factor (a measure of the static and thermal disorder), and the coordination number were subjected to least-squares refinement from a variety of starting positions and converged to the models summarized in Table 1.

RESULTS

Purified NTD Contains One Zinc for Two Protomers. We used X-ray fluorescence to identify metals associated with purified, recombinant NTD. The spectrum in Figure 2A reveals the presence of zinc above the signal in the buffer. Other metals, such as Cu, do not appear to be associated with the enzyme.

Table 1: Models for Zinc Coordination from EXAFS

	Zn-S ₄ ^a	Zn-S ₃ (N/O) ^a
sulfur–zinc distance (Å)	2.35	2.35
oxygen– or nitrogen–zinc distance (Å)		2.03
A ^b sulfur	0.009	0.005
A ^b nitrogen and oxygen		0.008
number of S ligands	3.93	3.03
number of N or O ligands		1.34
N_{ind} ^c	6.88	7.47
N_{pars}	4	7
ϕ_{EXAFS}	0.98	0.84
R_{EXAFS} (%)	37.71	32.93
ϵ_v^2	9.75	55.52

^a Bond valence sum calculations for Zn–S₄ model BVS = 1.95 and for Zn–S₃(N/O) BVS = 1.90; the expected value is 2.00. ^b Debye–Waller factor disorder parameter (Å²). ^c For parameter abbreviations, see the Materials and Methods.

The stoichiometric zinc content of NTD was then investigated using microPIXE. This method involves using a small diameter ($\sim 1 \mu\text{m}$) 2–3 MeV proton beam to induce characteristic X-ray emission from drops of liquid protein dried onto a Mylar film. These characteristic X-rays are then detected with high-energy resolution. The proton beam is scanned spatially, and two-dimensional maps of elemental content are produced by setting windows around peaks from specific elements in the X-ray spectrum and sorting those events into an xy grid. The profile of the emission data confirm that zinc is the principal metal present, with no other metals detectable (results not shown).

The microPIXE sulfur map clearly defines the position of the NTD protein droplet; the sulfur signal indicates the presence of the methionine and cysteine residues in the sample. Quantitative information is obtained by collecting spectra at selected points on the drop and also at a point on the backing foil. These spectra are analyzed to extract the areal density of each element of interest in the sample. The number of atoms of each element per protein molecule was computed from the ratio of that element to the sulfur measurement and knowledge of the number of cysteine and methionine residues in the protein (i.e., number of sulfur atoms per molecule).

Three points on the protein drop were measured for zinc and sulfur content, giving an average of 0.58 (± 0.07) atoms of zinc per NTD molecule (assuming 12 sulfurs in the molecule). The control experiment on the buffer alone confirmed that it made no contribution to the sulfur or zinc signals.

Chemical Structure of the Zinc Coordination Site. To characterize the metal ligands in the NTD, we used X-ray spectroscopy at the metal absorption edge (EXAFS). The oscillations in the scattering as a function of energy at the X-ray absorption edge of a metal arise from the back-scattering of emitted photoelectrons by the coordinating atoms, and the amplitude and frequency of these oscillations provide information about the nature, number, and distances of the metal–ligands. The scaled and normalized experimental EXAFS scan at the zinc K edge of NTD is shown in i and ii of Figure 2B (black traces) and compared with two models for metal coordination (red traces). The spectrum is qualitatively similar with that of other proteins with zinc–tetrathiol coordination (50).

The quantitative analysis of the EXAFS data used a number of different starting models to seek the best fit to

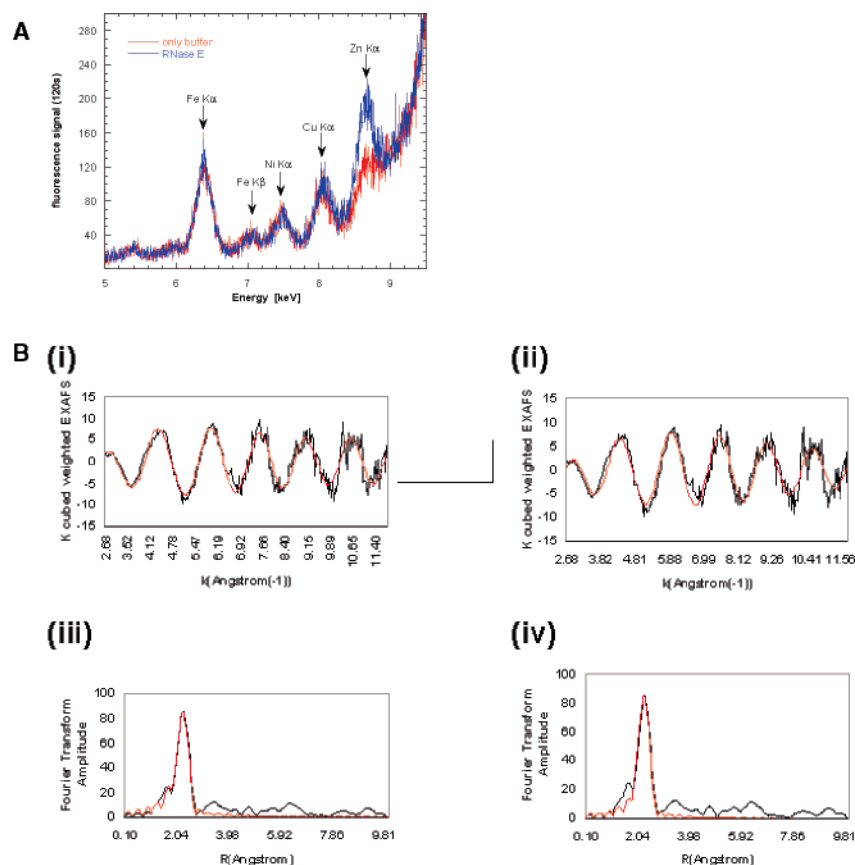


FIGURE 2: Metal analysis of the NTD. (A) X-ray fluorescence scan. The trace for the protein is shown in blue and the buffer alone, in red. The zinc content of the protein is significantly greater than for the buffer alone. (B) Spectroscopic analysis of metal coordination by the NTD. EXAFS data (experimental data, black line; theory, red line) for two models (i) Zn-S₃(N/O) three sulfurs and one lighter atom and (ii) Zn-S₄ four sulfurs. The corresponding Fourier transforms are shown in (iii) and (iv), respectively (experimental data, black line; theory, red line).

the experimental data. The curve-fitting analysis was restricted to single scattering from the first coordination shell. The Fourier transform of the EXAFS Zn K edge of NTD is shown in iii and iv of Figure 2B for the experimental data (black traces) and the two models (red traces). This clearly shows the first shell centered at roughly 2.2 Å. There is a partially resolved shoulder on the main peak near 2 Å.

The two models that gave the best fits to the EXAFS data were (i) Zn-S₃(N/O), consisting of a zinc with a shell of three equidistant sulfurs at 2.35 Å and an additional shell with a lighter atom (nitrogen or oxygen) as the fourth ligand at 2.03 Å ($\phi_{\text{EXAFS}} = 0.84$, $R_{\text{EXAFS}} = 32.93\%$, and $\epsilon_v^2 = 55.52$) and (ii) Zn-S₄, consisting of zinc with a single shell of four equidistant sulfurs at 2.35 Å ($\phi_{\text{EXAFS}} = 0.98$, $R_{\text{EXAFS}} = 37.71\%$, and $\epsilon_v^2 = 9.75$). The EXAFS fitting parameters for both models are summarized in Table 1.

The presence of conserved cysteines in the putative zinc-binding site together with the Zn-S₄ providing the best statistical fit to the EXAFS data and a marginally improved bond valence sum estimate led us to propose a Zn-Cys₄-binding site, although it does not entirely rule out a scheme such as Zn-Cys₃ with histidine or water as the fourth ligand.

Mutagenesis of the Putative Zinc-Binding Site. The EXAFS data suggest that each zinc is coordinated by at least three cysteine residues. In searching through the protein sequence, we identified two cysteine residues that are part of a conserved sequence motif, CPXCXGXG (Figure 1). Two such motifs could be used to create a tetrathiol coordination

scheme, as they do in the case of MutM and DnaJ. In those proteins, the two motifs form an intramolecular pair, but in RNase E, they would likely form an intermolecular pair as part of a dimerization interface.

In *E. coli* RNase E, the cysteine residues correspond to C404 and C407. Alanine substitutions were made for the presumptive C404 and C407 zinc ligands, individually, and both mutants were examined for zinc binding, oligomerization, catalytic activity, and RNA binding. Analysis by microPIXE revealed 0.25 (± 0.03) and 0.26 (± 0.03) atoms of zinc per NTD C404A and C407A mutant molecule, respectively, which are less than half of the metal stoichiometry of the wild-type protein. Both mutants were found to have 200-fold decreased activity relative to that of the wild-type enzyme for cleaving a 10-mer RNA substrate (Figure 3).

When the mutant forms are compared with the wild-type NTD, the mutant forms had a marked decrease in their elution volumes from size-exclusion chromatography, with both mutants eluting at a position consistent with a dimer, versus the tetramer observed for the wild-type protein. These masses were corroborated by analytical ultracentrifugation (AUC) (pink and green traces in Figure 4A), which showed that both of the mutants have a molecular mass of ~125 kDa. Similarly, nondissociating nanoflow-ESI mass spectrometry analysis of both the mutants gave spectra showing charge-state series that represent one species with an observed molecular mass of $124\,226 \pm 10$ Da for mutant

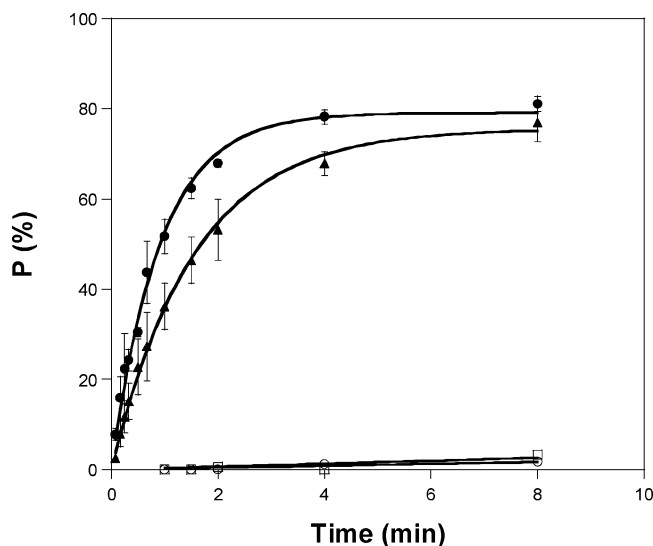


FIGURE 3: Enzymatic activity assay. Time course showing the cleavage of a 10-mer substrate as monitored by the rate of product release. Data shown for activity of NTD (●), diamide-treated NTD (▲), and mutants C404A (○) and C407A (□). Assay conditions are as detailed in the Materials and Methods.

C407A and $124\,063 \pm 21$ Da for mutant C404A (red traces in i and ii of Figure 4B). These correspond to the dimeric form of the protein in each case (theoretical mass of 123 704 Da for each mutant). As is common with this technique, the experimental mass observed is slightly greater than the theoretical expected mass of the protein because of the association of buffer molecules. Although the mutants were catalytically impeded, both could still bind a derivative of the 10-mer RNA in which the 2'-O was protected from cleavage by methyl groups, as observed by nondissociating nanoflow-ESI mass spectrometry (green traces in i and ii of Figure 4B). Upon addition of the RNA in slight stoichiometric excess, an extra two charge-state series were identified for both mutants. For C407A, series B with a mass of $127\,892 \pm 28$ Da and series C with a mass of $131\,762 \pm 50$ Da were observed, corresponding to the dimeric form of the protein with one and two RNA molecules bound, respectively (theoretical masses of 127 637 and 131 570 Da, respectively). Similarly, for C404A, series B with a mass of $127\,885 \pm 14$ Da and series C with a mass of $131\,881 \pm 42$ Da were observed, likewise corresponding to the dimeric form of the protein with one and two RNA molecules bound, respectively. The mutant dimers could therefore bind up to two molecules of the RNA, equivalent to one per monomer and exactly half the number bound to the wild-type tetrameric protein (31). Moreover, electrophoretic mobility shift assays indicate that the binding affinities of the two mutants and wild-type NTD are comparable, with all three having values of K_d between 1 and 2 μ M for an oligonucleotide substrate (results not shown). Therefore, the change in quaternary structure has not affected RNA binding.

Effects of Diamide Treatment on NTD. Diamide is a strong oxidizing agent which favors disulfide bond formation between spatially paired cysteine residues. In studies of the bacterial σ^{70} factor, diamide treatment has been shown to displace a structural zinc and cause formation of a disulfide link (51). Treatment of NTD with diamide causes complete loss of the zinc, as determined by microPIXE analysis.

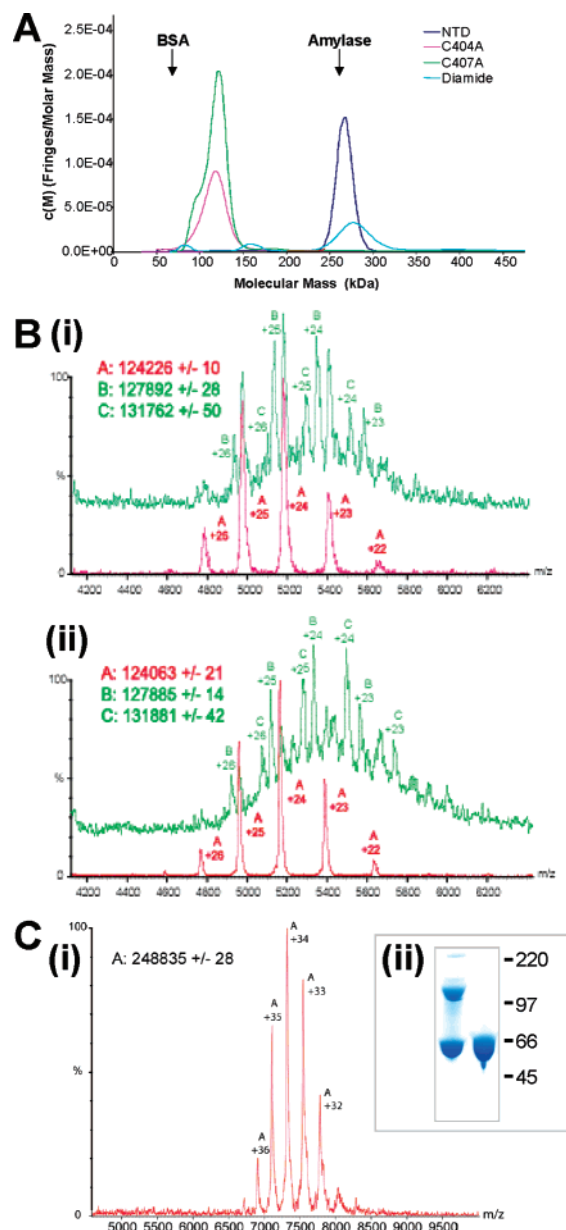


FIGURE 4: Oligomeric-state analysis. (A) Analytical ultracentrifugation analysis. The distribution of molecular masses of NTD (dark blue), mutants C404A (pink) and C407A (green), and the diamide-treated NTD (light blue) obtained from sedimentation velocity data are shown. For comparison, the position of the peaks obtained from analysis of BSA (67 kDa) and amylase (210 kDa) under the same conditions are shown. Data analysis was performed using Sedfit (60). (B) Nanoflow-ESI mass spectra of the NTD mutants in the absence and presence of RNA, recorded under nondissociating conditions. (i) ESI mass spectrum of C407A (red trace) and C407A after addition of RNA 10-mer (green trace), vertically offset from zero for clarity. Charge-state series A is assigned as the C407A dimer; B, as the C407A dimer with one RNA bound; and C, as the C407A dimer with two RNAs bound. (ii) ESI mass spectrum of C404A (red trace) and C404A after addition of RNA 10-mer (green trace), vertically offset from zero for clarity. Charge-state series A is assigned as the C404A dimer; B, as the C404A dimer with one RNA bound; and C, as the C404A dimer with two RNAs bound. (C) (i) Nanoflow-ESI mass spectrum of the diamide-treated NTD, recorded under nondissociating conditions. The charge-state series observed is assigned as the tetrameric form of the protein. (ii) SDS-PAGE analysis of diamide-treated NTD. The position of the molecular weight markers are shown. The left and right lanes correspond to diamide-treated NTD analyzed under reducing and nonreducing SDS-PAGE conditions, respectively. The monomeric NTD form, at ~ 66 kDa, and the dimeric species, at ~ 120 kDa, are labeled.

If the zinc metal plays a structural role in maintaining the tetramer, it might be expected that the diamide-treated material would be predominantly a dimer on account of the loss of metal. However, the treated protein was in fact observed to be a tetramer by size-exclusion chromatography, where the elution profile of the diamide-treated sample was observed to be the same as that of the wild-type NTD. Similarly, AUC (light blue trace in Figure 4A) also illustrated the tetrameric nature of the diamide-treated NTD, identifying it to have a molecular mass of ~ 270 kDa, close to the value obtained for analysis of the untreated NTD. Likewise, nondissociating nanoflow-ESI mass spectrometry analysis gave a spectrum showing a charge-state series that represents one species with an observed mass of $248\,835 \pm 28$ Da, corresponding to the tetrameric form of the protein (theoretical mass of 247 536 Da) (i of Figure 4C). This raises the question as to how the tetramer might be maintained.

We have proposed that the zinc-coordinating residues are in close proximity because they are likely to share a metal ion across a dimerization interface. Diamide treatment is likely to cross-link these residues across the interface, thus displacing the zinc while still maintaining the association of the quaternary structure. Consistent with this hypothesis, the diamide-treated NTD migrated as a dimer in a denaturing gel under nonreducing conditions, indicating that the two subunits are linked covalently. Only a monomer of NTD was seen under reducing conditions in which the disulfide cross links are broken (ii of Figure 4C).

The diamide-treated NTD was found to be nearly as active as the untreated protein (Figure 3). This suggests that the zinc is not required for catalytic activity; furthermore, it also suggests that the active site itself is not sensitive to oxidizing agents and is not likely to use cysteines as part of the catalytic mechanism.

DISCUSSION

We present evidence that the NTD, corresponding to a well-conserved portion of the protein, contains a structural zinc ion. EXAFS analysis has shown that the metal is most likely to be coordinated by the thiol groups of four cysteine residues. On the basis of microPIXE data, which give a ratio of 0.5 zinc atoms per NTD monomer, it appears that the zinc is shared between two protomers at a dimer interface. We have noted a conserved sequence motif, CPXCXG, that could provide two of the four thiol ligands for the zinc-binding site. Two such motifs would complete the required tetrahedral coordination. There is precedent for association of such motifs, as seen for example in the MutM and DnaJ zinc-binding sites (PDB codes 1EE8 and 1EXK). In these two proteins, zinc binding occurs *intramolecularly*, but we propose that in RNase E the same pattern (CXXCXXG) is used for *intermolecular* association to form a dimerization interface, the “Zn-link” motif (Figure 5). Similarly, a conserved CXXC motif is used in intermolecular zinc-mediated dimerization of Rad50 (52). A zinc-mediated dimerization interface occurs in endothelial nitric oxide synthase, although a different motif is used in this case (53).

On the basis of the conserved Cys motif sequence pattern that we identified and the effects of mutations, we predict that C404 and C407 coordinate the zinc and are involved in a metal-binding dimerization interface. We had shown earlier

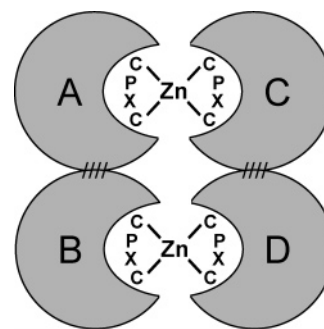


FIGURE 5: Schematic representation of the NTD tetramer with two nonequivalent subunit interfaces. NTD monomers are depicted by the grey circles. The “Zn-link” dimerization interface is shown with the zinc ligated through the residues of the conserved Cys motif. The protein–protein interface of the tetramer is indicated by the crosshatching. The individual subunits are labeled A, B, C, and D. Dimers of the type A–B and C–D were observed for the NTD mutant forms in which the zinc-mediated dimerization interface was lost. Dimers of the type A–C and B–D were observed under nonreducing conditions in a denaturing gel analysis of the diamide-treated NTD.

that NTD forms a homotetramer (31), and here, we find that mutations of the conserved C404 and C407 residues cause the tetramers to dissociate into dimers. We attribute this to the disruption of the metal-sharing interfaces in the mutant proteins (Figure 5). The fact that the C404A and C407A mutant proteins are stable dimers rather than monomers indicates that a second protein–protein interface is also present that is independent of the “Zn-link” (crosshatching in Figure 5). The tetrameric quaternary structure of wild-type NTD is therefore likely to be arranged as a dimer of dimers. The previous evidence from low-resolution crystal data was used to suggest a tetrameric assembly with 222 symmetry, and this restraint was used for a reconstruction of the NTD assembly from solution-scattering data as an idealized tetrahedron with all of the interaction surfaces equivalent (31). The current model of a dimer of dimers is still consistent with 222 symmetry, but suggests that the molecule does not have strict tetrahedral symmetry and that there are two nonequivalent interfaces.

The endogenous zinc from NTD could be removed completely by diamide treatment, as confirmed by microPIXE analysis. It was initially thought that this treatment would disrupt the tetramer in the same way that the mutations of C404A and C407A do. However, the diamide-treated NTD is still a tetramer, as identified by AUC and nondissociating nanoflow-ESI mass spectrometry, although it has lost the zinc entirely. The preservation of the quaternary structure might be explained by proximity of the conserved Cys residues of the putative zinc-binding dimerization interface, which would be capable of forming disulfide linkages across the interface under oxidizing conditions of diamide treatment (Figure 5). As shown in this figure, there is a second interaction site (crosshatched), and as a result, our model predicts a minimum ratio of 1:1 for cross-linked/monomeric species to preserve the tetramer in NTD in the absence of zinc. Consistent with this, an approximately 1:1 ratio was in fact observed under nonreducing conditions for the diamide-treated NTD separated under denaturing conditions in panel (ii) of Figure 4C.

The preparation of a zinc-free tetrameric form of NTD as well as Cys-motif mutant dimeric forms enabled us to

investigate the role of zinc and the quaternary structure on enzymatic activity. The data indicate that the quaternary structure of NTD is important for catalytic activity, with the zinc-free tetrameric form being almost as active as the wild-type NTD, whereas the dimeric Cys-motif mutants were impeded catalytically. The observation that the quaternary structure, mediated through a "Zn-link" interface, is vital to catalytic activity has also been observed for endothelial nitric oxide synthase (54). Could RNase E serve as a sensor of intracellular oxidative stress, in analogy with the anti- σ factor (51)? Our data indicate that this is unlikely, because a strong oxidizing agent has no measurable effect on its activity. Instead, it seems possible that the enzyme could serve as a direct sensor of zinc availability: under conditions of limiting zinc, RNase E would not readily form the catalytically active tetramer, with potential consequences for stability of particular transcripts.

Previous work indicated that wild-type tetrameric NTD is able to bind up to four molecules of 10-mer RNA, one for each subunit (31). The subunits of the mutant NTD dimers also each bind one RNA, illustrating that the quaternary structure is not important for RNA binding per se. However, as the mutant NTD dimers significantly lose activity, it seems likely that the catalytic site is supported by interfacial interactions, because these are disrupted in the mutant NTD dimers.

The relationship between RNase E quaternary structure and activity has been commented upon in previous studies. Coburn and Mackie (55) proposed that a hypothetical dimeric organization of RNase E could permit the interplay of binding and catalytic sites to effect a processive catalytic mode such that the binding of the 5' end of RNA (namely, the 5'-monophosphate) could occur at one protomer, with cleavage of the tethered substrate proceeding at the neighboring protomer. Evidence that the NTD exists as a tetrameric assembly indeed supports this hypothesis, as it would further facilitate processive activity. However, the observation that the Cys-motif mutants are dimeric and catalytically impeded indicates that the tetrameric arrangement of protomers is important for catalytic activity, in terms of cleaving the small RNA substrates used in this study. The quaternary structure therefore appears to support catalysis by facilitating communication between protomers or by maintenance of the active site.

ACKNOWLEDGMENT

We thank the staff of Daresbury SRS and the National Ion Beam Centre in Surrey, in particular Geoff Grime, for assistance with the use of the facilities.

REFERENCES

- Bernstein, J. A., Lin, P.-H., Cohen, S. N., and Lin-Chao, S. (2004) Global analysis of *Escherichia coli* RNA degradosome function using DNA microarrays, *Proc. Natl. Acad. Sci. U.S.A.* 101, 2758–2763.
- Lee, K., Bernstein, J. A., and Cohen, S. N. (2002) RNase G complementation of *rne* null mutation identifies functional interrelationships with RNase E in *Escherichia coli*, *Mol. Microbiol.* 43, 1445–1456.
- Apirion, D., and Lassar, A. B. (1978) A conditional lethal mutant of *Escherichia coli* which affects the processing of ribosomal RNA, *J. Biol. Chem.* 253, 1738–1742.
- Ono, M., and Kuwano, M. (1979) A conditional lethal mutation in an *Escherichia coli* strain with a longer chemical half life of mRNA, *J. Mol. Biol.* 129, 343–357.
- Mudd, E. A., Krisch, H. M., and Higgins, C. F. (1990) RNase E, an endoribonuclease, has a general role in the chemical decay of *Escherichia coli* mRNA: Evidence that *rne* and *ams* are the same genetic locus, *Mol. Microbiol.* 4, 2127–2135.
- Babitzke, P., and Kushner, S. R. (1991) The Ams (altered mRNA stability) protein and ribonuclease E are encoded by the same structural gene of *Escherichia coli*, *Proc. Natl. Acad. Sci. U.S.A.* 88, 1–5.
- Taraseviciene, L., Miczak, A., and Apirion, D. (1991) The gene specifying RNase E (*rne*) and a gene affecting mRNA stability (*ams*) are the same gene, *Mol. Microbiol.* 5, 851–855.
- Melefors, O., and von Gabain, A. (1991) Genetic studies of cleavage-initiated mRNA decay and processing of ribosomal 9S RNA show that the *Escherichia coli* *ams* and *rne* loci are the same, *Mol. Microbiol.* 5, 857–864.
- Huang, H., Liao, J., and Cohen, S. N. (1998) Poly (A)- and poly (U)-specific RNA 3' tail shortening by *Escherichia coli* ribonuclease E, *Nature* 391, 99–102.
- Kushner, S. R. (2002) mRNA decay in *Escherichia coli* comes of age, *J. Bacteriol.* 184, 4658–4665.
- Ow, M. C., and Kushner, S. R. (2002) Initiation of tRNA maturation by RNase E is essential for cell viability in *Escherichia coli*, *Genes Dev.* 16, 1102–1115.
- McDowall, K. J., and Cohen, S. N. (1996) The N-terminal domain of the *rne* gene product has RNase E activity and is non-overlapping with the arginine-rich RNA-binding site, *J. Mol. Biol.* 255, 349–355.
- Kido, M., Yamanaka, K., Mitani, T., Niki, H., Ogura, T., and Hiraga, S. (1996) RNase E polypeptides lacking a carboxy-terminal half suppress a *mukB* mutation in *Escherichia coli*, *J. Bacteriol.* 178, 3917–3925.
- Kaberdin, V. R., Miczak, A., Jakobsen, J. S., Lin-Chao, S., McDowall, K. J., and von Gabain, A. (1998) The endoribonucleolytic N-terminal half of *Escherichia coli* RNase E is evolutionarily conserved in *Synechocystis* sp. and other bacteria, but not the C-terminal half, which is sufficient for degradosome assembly, *Proc. Natl. Acad. Sci. U.S.A.* 95, 11637–11642.
- Aravind, L., and Koonin, E. V. (2001) A natural classification of ribonucleases, *Methods Enzymol.* 341, 3–28.
- Baginsky, S., Sheiman-Kotler, A., Liveanu, V., Yehudai-Resheff, S., Bellaou, M., Settlege, R. E., Shabanowitz, J., Hunt, D. F., Schuster, G., and Grisssem, W. (2001) Chloroplast PNPase exists as a homo-multimer enzyme complex that is distinct from the *Escherichia coli* degradosome, *RNA* 7, 1464–1475.
- Kanai, A., Oida, H., Matsuura, N., and Doi, H. (2003) Expression cloning and characterization of a novel gene that encodes the RNA-binding protein FAU-1 from *Pyrococcus furiosus*, *Biochem. J.* 372, 253–261.
- Li, Z., Pandit, S., and Deutscher, M. P. (1999) RNase G (CafA protein) and RNase E are both required for the 5' maturation of 16S ribosomal RNA, *EMBO J.* 18, 2878–2885.
- Wachi, M., Umitsuki, G., Shimizu, M., Takada, A., and Nagai, K. (1999) *Escherichia coli* *cafA* gene encodes a novel RNase, designated as RNase G, involved in processing of the 5' end of 16S rRNA, *Biochem. Biophys. Res. Commun.* 259, 483–488.
- Tock, M. R., Walsh, A. P., Carroll, G., and McDowall, K. J. (2000) The CafA protein required for the 5'-maturation of 16 S rRNA is a 5'-end-dependent ribonuclease that has context-dependent broad sequence specificity, *J. Biol. Chem.* 275, 8726–8732.
- Wachi, M., Umitsuki, G., and Nagai, K. (1997) Functional relationship between *Escherichia coli* RNase E and the CafA protein, *Mol. Gen. Genet.* 253, 515–519.
- Lee, K., Bernstein, J. A., and Cohen, S. N. (2002) RNase G complementation of *rne* null mutation identifies functional interrelationships with RNase E in *Escherichia coli*, *Mol. Microbiol.* 43, 1445–1456.
- Ow, M. C., Perwez, T., and Kushner, S. R. (2003) RNase G of *Escherichia coli* exhibits only limited functional overlap with its essential homologue, RNase E, *Mol. Microbiol.* 49, 607–622.
- Condon, C., and Putzer, H. (2002) The phylogenetic distribution of bacterial ribonucleases, *Nucl. Acids Res.* 30, 5339–5346.
- Lee, K., and Cohen, S. N. (2003) A *Streptomyces coelicolor* functional orthologue of *Escherichia coli* RNase E shows shuffling of catalytic and PNPase-binding domains, *Mol. Microbiol.* 48, 349–360.

26. Carpousis, A. J. (2002) The *Escherichia coli* RNA degradosome: Structure, function, and relationship to other ribonucleolytic multienzyme complexes, *Biochem. Soc. Trans.* **30**, 150–155.
27. Carpousis, A. J., van Houwe, G., Ehretsmann, C., and Krisch, H. M. (1994) Copurification of *Escherichia coli* RNase E and PNPase: Evidence for a specific association between two enzymes important in RNA processing and degradation, *Cell* **76**, 889–900.
28. Py, B., Higgins, C. F., Krisch, H. M., and Carpousis, A. J. (1996) A DEAD-box RNA helicase in the *Escherichia coli* RNA degradosome, *Nature* **381**, 169–172.
29. Miczak, A., Kaberdin, V. R., Wei, C.-L., and Lin-Chao, S. (1996) Proteins associated with the RNase E in a multicomponent ribonucleolytic complex, *Proc. Natl. Acad. Sci. U.S.A.* **93**, 3865–3869.
30. Bernstein, J. A., Lin, P., Cohen, S. N., and Lin-Chao, S. (2004) Global analysis of *Escherichia coli* RNA degradosome function using DNA microarrays, *Proc. Natl. Acad. Sci. U.S.A.* **101**, 2758–2763.
31. Callaghan, A. J., Grossmann, J. G., Redko, Y. U., Ilag, L. L., Moncrieffe, M. C., Symmons, M. F., Robinson, C. V., McDowall, K. J., and Luisi, B. F. (2003) Quarternary structure and catalytic activity of the *Escherichia coli* ribonuclease E amino-terminal catalytic domain, *Biochemistry* **42**, 13848–13855.
32. Schubert, M., Edge, R. E., Lario, P., Cook, M. A., Strynadka, N. C. J., Mackie, G. A., and McIntosh, P. M. (2004) Structural characterization of the RNase E S1 domain and identification of its oligonucleotide-binding and dimerization interfaces, *J. Mol. Biol.* **341**, 37–54.
33. Diwa, A. A., Jiang, X., Schapira, M., and Belasco, J. G. (2002) Two distinct regions on the surface of an RNA-binding domain are crucial for RNase E function, *Mol. Microbiol.* **46**, 959–969.
34. Tomcsányi, T., and Apirion, D. (1985) Processing enzyme ribonuclease E specifically cleaves RNA I. An inhibitor of primer formation in plasmid DNA synthesis, *J. Mol. Biol.* **185**, 713–720.
35. Lin-Chao, S., and Cohen, S. N. (1991) The rate of processing and degradation of antisense RNAI regulates the replication of ColEI-type plasmids *in vivo*, *Cell* **65**, 1233–1242.
36. Mackie, G. A. (1998) Ribonuclease E is a 5'-end-dependent endonuclease, *Nature* **395**, 720–724.
37. Jiang, X., and Belasco, J. G. (2004) Catalytic activation of multimeric RNase E and RNase G by 5'-monophosphorylated RNA, *Proc. Natl. Acad. Sci. U.S.A.* **101**, 9211–9216.
38. Redko, Y., Tock, M. R., Adams, C. J., Kaberdin, V. R., Grasby, J. A., and McDowall, K. J. (2003) Determination of the catalytic parameters of the N-terminal half of *Escherichia coli* ribonuclease E and the identification of critical functional groups in RNA substrates, *J. Biol. Chem.* **278**, 44001–44008.
39. Sobott, F., Hernandez, H., McCammon, M. G., Tito, M. A., and Robinson, C. V. (2002) A tandem mass spectrometer for improved transmission and analysis of large macromolecular assemblies, *Anal. Chem.* **74**, 1402–1407.
40. Ilag, L. L., Westblade, L. F., Deshayes, C., Kolb, A., Busby, S. J., and Robinson, C. V. (2004) Mass spectrometry of *Escherichia coli* RNA polymerase: Interactions of the core enzyme with $\sigma 70$ and Rsd protein, *Structure* **12**, 269–275.
41. Grime, G. W., Dawson, M., Marsh, M., McArthur, I. C., and Watt, F. (1991) The Oxford submicron nuclear microscopy facility, *Nucl. Instrum. Methods Phys. Res., Sect. B* **54**, 52–63.
42. Garman, E. (1999) Leaving no element of doubt: Analysis of proteins using microPIXE, *Structure* **7**, R291–R299.
43. Johansson, S. A. E., Campbell, J. L., and Malmqvist, K. G. (1995) *Particle Induced X-ray Emission Spectrometry*, Wiley and Sons, New York.
44. Farrow, R. C., Headspith, J., Dent, A. J., Dobson, B. R., Bilsborrow, R. L., Ramsdale, C. A., Stephenson, P. C., Brierley, S., Derbyshire, G. E., Sangsingkeow, P., and Buxton, K. (1998) Initial data from the 30-element ORTEC HPGe detector array and the XSPRESS pulse-processing electronics at the SRS, Daresbury Laboratory, *J. Synchrotron Radiat.* **5**, 845–847.
45. Morrell, C., Baines, J. T. M., Campbell, J. W., Daikun, G. P., Dobson, B. R., Greaves, G. N., and Hasnain, S. S. (1989) *EXAFS Users' Manual*, SERC Daresbury Laboratory, Warrington, U.K.
46. Binsted, N., Gurman, S. J., Campbell, J. W., and Stephenson, P. (1991) *SERC Daresbury Laboratory Program EXCURVE*, SERC Daresbury Laboratory, Warrington, U.K.
47. Binsted, N., Strange, R. W., and Hasnain, S. S. (1992) Constrained and restrained refinement in EXAFS data analysis with curved wave theory, *Biochemistry* **31**, 12117–12125.
48. Strange, R. W., Reinhammar, B., Murphy, L. M., and Hasnain, S. S. (1995) Structural and spectroscopic studies of the copper site of stellacyanin, *Biochemistry* **34**, 220–231.
49. Brown, I. D. (1996) VALENCE: A program for calculating bond valences, *J. Appl. Crystallogr.* **29**, 479–480.
50. Vanamee, E. S., Hsieh, P., Zhu, Z., Yates, D., Garman, E., Xu, S., and Aggarwal, A. K. (2003) Glucocorticoid receptor-like Zn(Cys)₄ motifs in BstII restriction endonuclease, *J. Mol. Biol.* **334**, 595–603.
51. Li, W., Bottrill, A. R., Bibb, M. J., Buttner, M. J., Paget, M. S. B., and Kleanthous, C. (2003) The role of zinc in the disulphide stress-regulated anti- σ factor RsrA from *Streptomyces coelicolor*, *J. Mol. Biol.* **333**, 461–472.
52. Hopfner, K.-P., Craig, L., Moncalian, G., Zinkel, R. A., Usui, T., Owen, B. A. L., Karcher, A., Henderson, B., Bodmer, J.-L., McMurray, C. T., Carney, J. P., Petrini, J. H. J., and Tainer, J. A. (2002) The Rad50 zinc-hook is a structure joining Mre11 complexes in DNA recombination and repair, *Nature* **418**, 562–565.
53. Raman, C. S., Li, H., Martasek, P., Kral, V., Masters, B. S. S., and Poulos, T. L. (1998) Crystal structure of constitutive endothelial nitric oxide synthase: A paradigm for pterin function involving a novel metal center, *Cell* **95**, 939–950.
54. Ravi, K., Brennan, L. A., Levic, S., Ross, P. A., and Black, S. M. (2004) S-Nitrosylation of endothelial nitric oxide synthase is associated with monomerization and decreased enzyme activity, *Proc. Natl. Acad. Sci. U.S.A.* **101**, 2619–2624.
55. Coburn, G. A., and Mackie, G. A. (1999) Degradation of mRNA in *Escherichia coli*: An old problem with some new twists, *Prog. Nucl. Acid Res. Mol. Biol.* **62**, 55–108.
56. Callaghan, A. J., Aurikko, J. P., Ilag, L. L., Grossmann, J. G., Chandran, V., Kuhnel, K., Poljak, L., Carpousis, A. J., Robinson, C. V., Symmons, M. F., and Luisi, B. F. (2004) Studies of the RNA degradosome-organizing domain of the *Escherichia coli* ribonuclease RNase E, *J. Mol. Biol.* **340**, 965–979.
57. Vanzo, N. F., Li, Y. S., Py, B., Blum, E., Higgins, C. F., Raynal, L. C., Krisch, H. M., and Carpousis, A. J. (1998) Ribonuclease E organises the protein interactions in the *Escherichia coli* RNA degradosome, *Gen. Dev.* **12**, 2770–2781.
58. Higgins, D., Thompson, J., and Gibson, T. J. (1994) CLUSTAL W: Improving the sensitivity of progressive multiple sequence alignment through sequence weighting, position-specific gap penalties, and weight matrix choice, *Nucleic Acids Res.* **22**, 4673–4680.
59. Gouet, P., Courcelle, E., Stuart, D. I., and Metoz, F. (1999) ESPript: Multiple sequence alignments in PostScript, *Bioinformatics* **15**, 305–308.
60. Schuck, P. (2000) Size-distribution analysis of macromolecules by sedimentation velocity ultracentrifugation and lamm equation modeling, *Biophys. J.* **78**, 1606–1619.